Optical Engineering 44(2), 023602 (February 2005)

# Laser beam profiling with extended-image-range techniques

**R. González-Moreno**
**J. A. Quiroga,** MEMBER SPIE
**J. Alonso**
**E. Bernabeu**
Universidad Complutense de Madrid
Departamento de Optica
Ciudad Universitaria S/N
28040 Madrid, Spain
E-mail: rgmoreno@fis.ucm.es

**Abstract.** A method to enlarge the dynamic range of a CCD-based laser beam profiler is presented. The method is based on extended-image-range techniques. The algorithm that generates the extended-irradiance-range image is described in detail. An equivalent dynamic range and number of bits are defined and computed for the new profiling system. To test the method, experimental measurements of the principal widths of the output beam from a single-mode optical fiber have been made, as well as the Fraunhofer diffraction pattern of a 200-$\mu$m pinhole back-illuminated by a HeNe laser. *© 2005 Society of Photo-Optical Instrumentation Engineers.* [DOI: 10.1117/1.1840931]

Paper 040178 received Mar. 31, 2004; revised manuscript received Jul. 13, 2004; accepted for publication Jul. 16, 2004; published online Jan. 21, 2005.

## 1 Introduction

Laser applications cover a wide range of fields. In particular there are many scientific and technological applications where the spatial irradiance distribution of a laser beam profile must be measured, for example, inertial fusion, laser machining, and medical uses of lasers such as LASIK surgery.[1] Complete beam characterization—both beam propagation and beam profile—requires the computation of the second and higher moments of the transverse irradiance distribution, which are very sensitive to the details of the beam tails and the noise of the acquired irradiance map. For this reason, large dynamic range of the measuring system is essential for the beam characterization.

Commercial setups[2] are mainly based on electronic detection of light. Among them we can distinguish between two philosophies: mechanical scanning instruments and camera-based systems. The first ones usually consist of a rotating drum containing a knife-edge, slit, or pinhole that moves in front of a single wide-area detector. On the other hand, camera-based profilers acquire a 2-D image corresponding to the spatial irradiance distribution that reaches the detector without mechanical scanning devices. The most frequently used cameras are silicon-based ones. Among them, due to their high quality, CCD-based cameras are the first choice in laser beam profiling applications.

The main drawback of CCD-based beam profilers is their limited dynamic range. For this reason, if we use a standard CCD with an 8-bit digitizer, even if there is an electronic shutter to control the integration time, it is necessary to use neutral filters in order to attenuate the beam until the maximum irradiance is below the saturation level of the CCD. However, the necessary attenuation means that some parts of the irradiance distribution decrease below the threshold level, possibly losing the information associated with the laser beam tails. If we wish to measure the first moments of the laser beam, this loss will be of minor importance, because the tails make a negligible contribution to the first moments. However, if the second moments and above are the parameters to be measured, the tails of the laser beam are of great importance. In consequence, for small-dynamic-range systems it is not possible to capture the complete relevant irradiance distribution.

In a different context the dynamic range problem also appears in imaging systems where the scene has high contrast.[3] To solve this problem several methods have been proposed.[3–5] Mainly they consist in combining images of the same scene captured with different exposure times. This technique is known as extended-intensity-range imaging.[3]

In this work we propose the application of an extended-range imaging technique to improve the laser beam profiling with a CCD-based setup. In particular we show how the dynamic range affects the measurement of the second moment and how we solve this problem by using extended-range imaging. Also we estimate the equivalent dynamic range achievable with a standard measurement system.

This work is organized as follows. In Sec. 2 we briefly describe the extended-intensity-range imaging algorithm and explicitly compute the equivalent dynamic range and the equivalent number of bits as a function of the dynamic range of the CCD camera. In Sec. 3 we show the dependence of the principal widths of a laser beam as a function of the bit depth achieved with the extended dynamic range. Conclusions are presented in Sec. 4.

## 2 Extended-Intensity-Range Algorithm. Equivalent Number of Bits

For the sake of completeness we briefly introduce the extended-range image method. A CCD camera generates a voltage level proportional to the charge stored in each pixel. Following Holst,[6] the saturation level $V_S$ is the voltage level generated when the charge well of the MOS capacitors saturates, and is proportional to the saturation energy density $E_S$. On the other hand, the noise determines the threshold level $V_{TH}$. Specifically, if $V_{noise}$ is the output rms noise, then $V_{TH}=V_{noise}$. The threshold $V_{TH}$ is also proportional to the minimum measurable energy density, $E_{TH}$. If we deal with uncooled cameras, this noise level is mainly determined by the thermal noise. For other kinds of devices, such as CMOS sensor imagers, $V_S$ and $V_{TH}$ are still defined, but with a slightly different physical origin.

The irradiance response of a CCD can be modeled in first approximation as

$$V(\mathbf{r}) = aE(\mathbf{r}) = aJ(\mathbf{r})T, \tag{1}$$

where $V$ is the generated voltage, $E$ is the spatial energy density, $J$ is the incident irradiance distribution ($\mathbf{r}$ denotes the spatial dependence of these quantities), $a$ is the average responsivity (in this simple model we are not considering either spatial or integration-time dependence), and $T$ is the integration time. This model is supported by the linearity of the CCD light detection physics. Afterwards, this voltage signal is digitized by the image-processing board, and a digital image $G(\mathbf{r})$ is generated. In order to take full advantage of the digitizer's dynamic range, its gain and offset are set so that the zero gray level is obtained for energy values $E \leqslant E_{\mathrm{TH}}$, whereas the maximum gray level, $2^N - 1$ for an $N$-bit digitizer, is obtained when the energy density reaches the saturation level, $E = E_{\mathrm{S}}$. With these settings, and assuming valid the linear model (1), the relationship between energy density and gray level is given by

$$E(\mathbf{r}) = \frac{E_{\mathrm{S}} - E_{\mathrm{TH}}}{2^N - 1} G(\mathbf{r}) + E_{\mathrm{TH}}, \tag{2}$$

that is,

$$G(\mathbf{r}) = S[E(\mathbf{r}) - E_{\mathrm{TH}}], \tag{3}$$

where $S = (2^N - 1)/(E_{\mathrm{S}} - E_{\mathrm{TH}})$ is the sensitivity, which is the reciprocal of the energy density interval $\delta E$ corresponding to each gray level. The dynamic range of the CCD is given by $\mathrm{DR} = E_{\mathrm{S}}/E_{\mathrm{TH}}$ [or $20 \log_{10}(E_{\mathrm{S}}/E_{\mathrm{TH}})$, when expressed in decibels]. Equation (2) can be rewritten as

$$E(\mathbf{r}) = \frac{1}{S}[G(\mathbf{r}) + G_0], \tag{4}$$

where $G_0 = (2^N - 1)/(\mathrm{DR} - 1)$ is the number of gray levels that would fit under $E_{\mathrm{TH}}$, that is, $E_{\mathrm{TH}}/\delta E$.

For a given integration time $T$, the irradiance can be obtained from Eq. (4) as

$$J(\mathbf{r}) = \frac{1}{ST}[G(\mathbf{r}) + G_0]. \tag{5}$$

However, Eq. (4) is only valid for irradiances within the interval $\Delta J_T = [E_{\mathrm{TH}}/T, E_{\mathrm{S}}/T]$. Outside these limits the information is lost. In case the irradiance distribution to be measured exceeds these limits, a single digital image will represent a truncated version of this distribution. If we set the integration time small enough so that the maximum irradiance in the image equals $E_{\mathrm{S}}/T$, we will avoid CCD saturation. However, all the information below $E_{\mathrm{TH}}/T$ (which corresponds with the zero gray level) will be lost. With a fixed integration time $T$, a similar effect can be obtained by using neutral filters to reduce the maximum irradiance to the value $E_{\mathrm{S}}/T$.

The solution proposed in the literature for this problem[3] is the acquisition of several digital images with different integration times $T_i$ ($i = 1,...,M, T_i > T_{i+1}$):

$$J_i(\mathbf{r}) = \frac{1}{ST_i}[G_i(\mathbf{r}) + G_0]. \tag{6}$$

All these images describe the same irradiance distribution, but each one is valid within an interval $\Delta J_i$ with limits given by $E_{\mathrm{TH}}/T_i$ and $E_{\mathrm{S}}/T_i$. In the region where $J_i$ and $J_{i+1}$ overlap, they are identical. Also, the irradiance step $\delta J$ corresponding to a digitalization interval depends on the integration time, $\delta J_i = \delta E/T_i$. The smallest step is achieved with the longer integration time, $T_1$.

We use the letter $\mathcal{J}$ to denote the irradiance values obtained when $\delta J_1$ is used as the irradiance unit, so that we have the equalities

$$\mathcal{J}_i(\mathbf{r}) = \frac{J_i}{\delta J_1} = \frac{T_1}{T_i}[G_i(\mathbf{r}) + G_0], \tag{7}$$

which are valid within the intervals

$$\Delta \mathcal{J}_i = \frac{\Delta J_i}{\delta J_1} = \frac{T_1}{T_i}[G_0, G_0 + 2^N - 1]. \tag{8}$$

Taking these intervals into account, the images can be now assembled into an extended-range image. The available integration times $\{T_i\}$ can be obtained directly from the camera manufacturer. In the interest of precision, however, as proposed in Ref. 3, an experimental calibration can be carried out by means of the acquisition of an irradiance distribution with two different integration times. A pixel with position $\mathbf{r}_{nm}$ is represented as a point whose coordinates are the gray levels obtained with the integration times $T_i$ and $T_{i-1}$, namely, $(G_i(\mathbf{r}_{nm}), G_{i-1}(\mathbf{r}_{nm}))$. The slope $\alpha_i$ of the line joining any two pixels $\mathbf{r}_{nm}$ and $\mathbf{r}_{\nu\mu}$ is the quotient between the integration times, $T_{i-1}/T_i$. To take into account the number of pixels for which the two gray levels are identical, a two-dimensional histogram can be created, such as the one shown in Fig. 1. To accurately determine $\alpha_i$, a linear fitting is made with all the pixels for which the irradiance intervals $\Delta J_{i-1}$ and $\Delta J_i$ overlap, that is, for all the pixels for which the energy density is above $E_{\mathrm{TH}}$ and below $E_{\mathrm{S}}$ for both integration times. Beginning with integration times $T_1$ and $T_2$, the remaining quotients can be obtained by repeating the method.

The overlapping of the irradiance interval $\Delta J$ is important not only to calibrate the camera integration times, but also to create the extended-range image. To evaluate the admissible difference between consecutive images taken with different integration times and minimize the number of images, we have quantified the overlapping by means of a new parameter, $\beta$. This is defined as the common portion of the irradiance intervals divided by the total irradiance range covered by them,

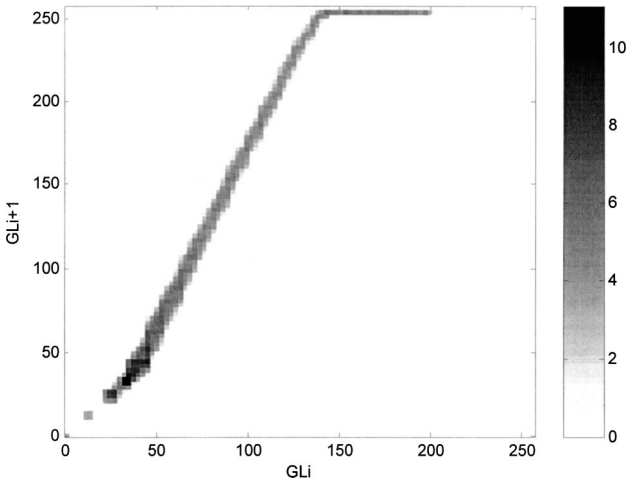


**Fig. 1** Two-dimensional histogram for exposure times $T_1 = 1/50$ s and $T_2 = 1/125$ s.

$$\beta_i = \frac{\frac{E_S}{T_{i-1}} - \frac{E_{TH}}{T_i}}{\frac{E_S}{T_i} - \frac{E_{TH}}{T_{i-1}}} = \frac{DR - \alpha_i}{\alpha_i DR - 1}. \tag{9}$$

Equation (8) indicates that low values of $\alpha_i$ imply large overlap between the irradiance intervals $\Delta J_{i-1}$ and $\Delta J_i$. As an example, the available integration times, as well as the slope and overlap resulting from them, are presented in Table 1 for the BeamStar CCD beam profiler system.[7] The overlap parameter varies in the range $\beta_i \approx 40\%$ to 80%, which means that using all the integration times gives rise to a high level of redundancy. On the other hand, too few (and too different) integration times can lead to negative values of $\beta$. When that happens, the irradiance intervals do not overlap and there is a loss of information.

Once the images $G_i$ are obtained and the scaled irradiance $\mathcal{J}_i$ for each integration time is computed from Eq. (7), the final extended range irradiance image can be computed as

**Table 1**

| $i$ | $T_i$ (s) | $\alpha_i$ | $\beta_i$(%) |
|---|---|---|---|
| 1 | 1/10 | | |
| 2 | 2/25 | 1.250 | 80 |
| 3 | 3/50 | 1.333 | 75 |
| 4 | 1/25 | 1.500 | 66 |
| 5 | 1/50 | 2.000 | 49 |
| 6 | 1/60 | 1.200 | 83 |
| 7 | 1/125 | 2.083 | 47 |
| 8 | 1/250 | 2.000 | 49 |
| 9 | 1/500 | 2.000 | 49 |
| 10 | 1/1000 | 2.000 | 49 |
| 11 | 1/2000 | 2.000 | 49 |
| 12 | 1/4000 | 2.000 | 49 |
| 13 | 1/10000 | 2.500 | 39 |

$$\mathcal{J}_{ER}(\mathbf{r}) = \begin{cases} \mathcal{J}_1(\mathbf{r}) & \text{if } \mathcal{J}_1(\mathbf{r}) \in \left[ G_0, \frac{T_1}{T_2} G_0 \right], \\ \mathcal{J}_2(\mathbf{r}) & \text{if } \mathcal{J}_2(\mathbf{r}) \in \left[ \frac{T_1}{T_2} G_0, \frac{T_1}{T_3} G_0 \right], \\ \vdots & \\ \mathcal{J}_M(\mathbf{r}) & \text{if } \mathcal{J}_M(\mathbf{r}) \in \left[ \frac{T_1}{T_M} G_0, \frac{T_1}{T_M} (G_0 + 2^N - 1) \right]. \end{cases} \tag{10}$$

In this formula, the extended scaled irradiance $\mathcal{J}_{ER}$ is equated to the scaled irradiance distribution $\mathcal{J}_i$ in the interval from the left of $\Delta\mathcal{J}_i$ to the left of $\Delta\mathcal{J}_{i+1}$, except for the last irradiance value, $\mathcal{J}_M$, which is equated to $\mathcal{J}_{ER}$ over the whole interval $\Delta\mathcal{J}_M$. Possibly this is the simplest way to assemble the extended irradiance image. More sophisticated methods can be used, with statistical methods (average, weighted average, or similar) to join the irradiance maps in the overlapping regions.

The dynamic range of this extended range image, $DR_{ER}$, can be calculated as a function of the dynamic range of the CCD camera and the linear relations between different sensitivities. For the extended-range irradiance image, the dynamic range is given by

$$DR_{ER} = \frac{\max(\mathcal{J}_M)}{\min(\mathcal{J}_1)}. \tag{11}$$

Substituting Eq. (7) into (11), we obtain

$$DR_{ER} = \frac{T_1}{T_M} \frac{(2^N - 1) + G_0}{G_0} = \frac{T_1}{T_M}(DR - 1) + 1 \approx \frac{T_1}{T_M} DR. \tag{12}$$

When expressed in decibels, the extended-range technique adds $20 \log_{10}(T_1/T_M)$ to the standard dynamic range. For example, if we use integration times $T_1 = 1/50$ s and $T_M = 1/10{,}000$ s, a CCD camera with a dynamic range of 56 dB will yield an extended-range irradiance image with 102 dB, a 46-dB increase.

Following Holst,[6] the dynamic range can be expressed in the form of the equivalent number of bits as

$$N_{eq} = \log_2 \frac{DR_{ER}}{\sqrt{12}}, \tag{13}$$

where it is assumed that the system noise is smaller than the least-significant bit of the analog-to-digital converter. Thus for the preceding example we have $N_{eq} = 7$ bits for the 56-dB CCD camera and $N_{eq} = 15$ bits for the extended-dynamic-range image. In consequence, a common low-cost image acquisition system (CCD and framegrabber) of 7 bits can be transformed in a 15-bit system using the extended irradiance range imaging technique.

It is worth to mention that for the preceding example, there is 0.3% overlap between the irradiances $\mathcal{J}_1$ and $\mathcal{J}_M$, so only two integration times (and therefore two digital images) are sufficient for a 46-dB increment in the dynamic range. Such a small overlap can be interpreted as almost perfect concatenation between the two irradiance ranges

represented by the digital images. However, due to problems associated with high and low gray levels, such as blooming and nonlinearity of the irradiance response, in practical applications it is worthwhile to have some amount of overlapping, which allows one to crop high and low gray levels for each digital image $G_i$, and also gives more degrees of freedom to assemble the extended-range irradiance image $\mathcal{J}_{\mathrm{ER}}$.

## 3 Experimental Results. Measurement of the Principal Widths of the Output Beam from a Single-Mode Optical Fiber

In the previous section we have shown that we can enlarge the dynamic range of a standard CCD laser beam profiler by merging images with different exposure times. In this section we show how the extended-intensity-range imaging technique can improve the characterization of a laser beam.

One of the most important parameters for the characterization a laser beam is the beamwidth.[8] There are different criteria for the definition of this width, many of them being based on the fraction of energy contained within a certain area, which are very convenient for cutting and welding applications. As a drawback, there are no propagation laws for the width defined by energy content criteria. It is the beam characterization based on the first and second moments of the transverse irradiance distribution that allows one to model beam propagation through first-order (ABCD) optical systems. The main quantity in this theory is the width tensor,[9,10] which is defined in terms of the second irradiance moments by

$$W^2 = 4\left[\begin{pmatrix} \langle x^2\rangle & \langle xy\rangle \\ \langle xy\rangle & \langle y^2\rangle \end{pmatrix} - \begin{pmatrix} \langle x\rangle \\ \langle y\rangle \end{pmatrix}(\langle x\rangle \ \ \langle y\rangle)\right], \tag{14}$$

where the $m+n$'th moment of the irradiance distribution $J(x,y)$ is given by

$$\langle x^m y^n\rangle = \frac{\int_{-\infty}^{\infty}\int_{-\infty}^{\infty} x^m y^n J(x,y)\,\mathrm{d}x\,\mathrm{d}y}{\int_{-\infty}^{\infty}\int_{-\infty}^{\infty} J(x,y)\,\mathrm{d}x\,\mathrm{d}y}. \tag{15}$$

The width tensor defined by Eq. (14) is referred to the laboratory system. Following Ref. 11, the principal directions are defined as those of the orientation that zeroes the nondiagonal elements of the tensor $W^2$. If we rotate the coordinate system to align the axes with the principal directions, the width tensor becomes diagonal. The elements of the diagonal are the squares of the so-called principal widths. As the width tensor is nonnegative, the eigenvalues will be the squares of principal widths and the eigenvectors will define the principal directions.

The experimental setup consists of a laser diode coupled into a single-mode optical fiber whose output is detected by a CCD camera. In this case, the output beam can be well approximated by a Gaussian distribution.[12] The CCD camera has a computer-controlled electronic shutter that permits it to obtain images with different integration times.

Once we have acquired the set of images with different integration times and applied the extended-range algorithm to obtain the final spatial distribution of irradiance, we calculate the principal widths using a numerical approximation of Eq. (11) given by

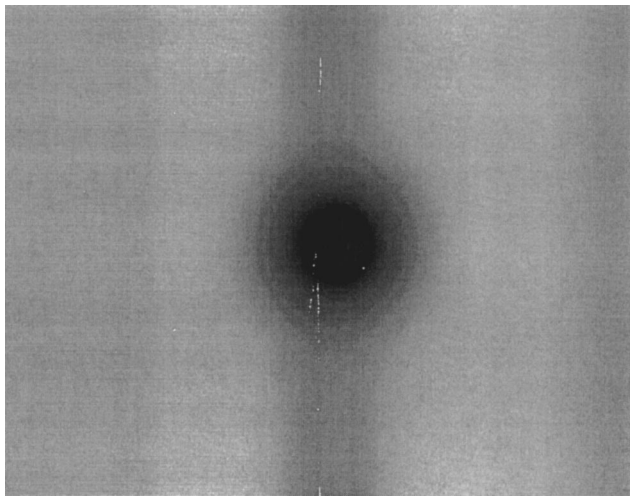

**Fig. 2** A logarithmic representation of a single image with 1/10,000 s of integration time.

$$\langle x^m y^n\rangle = \frac{\Sigma_{i,j} x_{i,j}^m y_{i,j}^n \mathcal{J}_{i,j}^*}{\Sigma_{i,j}\mathcal{J}_{i,j}^*}. \tag{16}$$

These sums are extended over all pixels of the matrix of detectors. Background subtraction in the irradiance map (whether it is direct or extended-range) is very important for the calculation of the spatial irradiance moments of a light beam.[13–16] Most CCD cameras produce a smoothly structured background (also called offset). For this reason, we have fitted the background to a fourth-order polynomial surface. In Eq. (16) the asterisk means that we have subtracted the background of the measured irradiance distribution.

There are in our system 13 available integration times (1/10,000, 1/4000, 1/2000, 1/1000, 1/500, 1/250, 1/125, 1/60, 1/50, 1/25, 3/50, 2/25, and 1/10 s). To show the improvement of the measurements of the second moments, we have generated 12 extended-range images with increasing values of the total number of integration times, $M$.

Figure 2 shows the irradiance distribution obtained with the smallest integration time, 1/10,000 s. A vertical structure appears in the image, distorting the beam. This smear is an artifact of our acquisition system, produced by intense and concentrated sources, and will introduce a severe error in the second moment if a single-exposure-time image is used. There are higher-quality CCD systems in which this vertical blooming is greatly reduced. We show below that the proposed technique will remove this artifact, allowing the use of cheaper cameras.

In Fig. 3 we present the results of the measurement of the principal widths as a function of the equivalent number of bits calculated with Eqs. (12) and (13), where the crosses and the dots represent the horizontal and vertical widths, respectively. The behavior of the measured principal widths is different along the two principal directions. For the horizontal width, the increase of dynamic range produces an

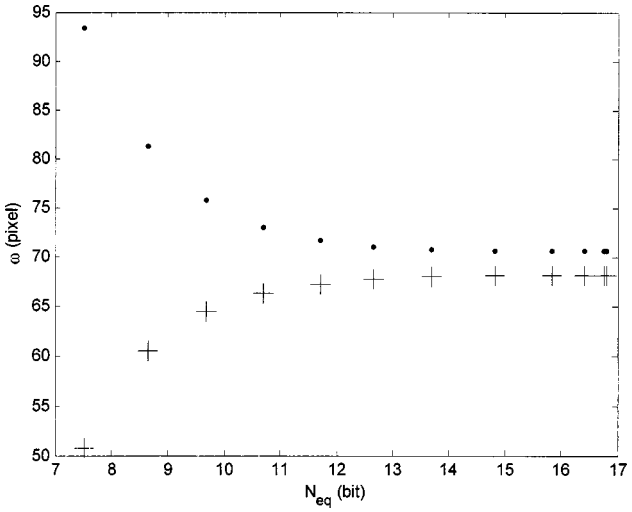


**Fig. 3** Principal widths calculated from different sets of images with increasing dynamic range. The dots represent the principal width in the vertical direction, and the crosses in the horizontal direction.

increase of the measured value. This is expected, as the lack of dynamic range cuts off the beam's tails, which have an important effect on the width. As the dynamic range increases, the tail of the beam emerges from the background noise (structured background has been removed). In other words, the use of longer integration times allows the irradiance at the beam tails to sensitize the pixels with energy densities larger than $E_{\mathrm{TH}}$. The extended-range technique allows the use of large integration times, avoiding saturation of the central peak.

The vertical width behaves differently. The vertical smear structure causes the width to be overestimated. As this smear does not depend on the integration time, its effect on the vertical width decreases as the dynamic range is increased.

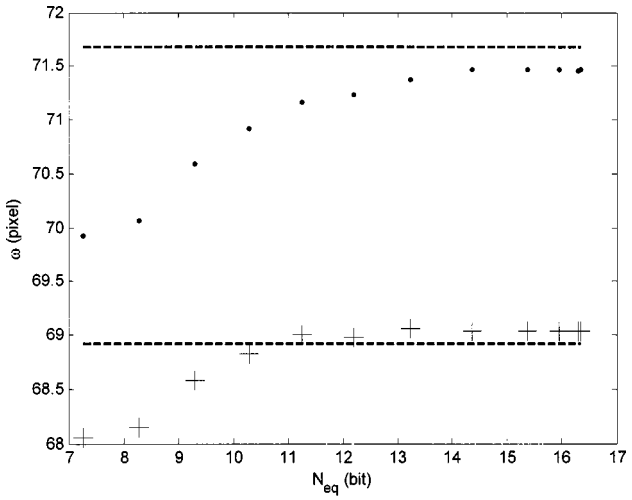


**Fig. 4** Evolution of the principal widths when the dynamic range is increasing and the method to eliminate the spurious structure is applied. The dots represent the principal width in the vertical direction, and the crosses in the horizontal direction. The horizontal dashed lines describe the asymptotic behavior of the results shown in Fig. 3.

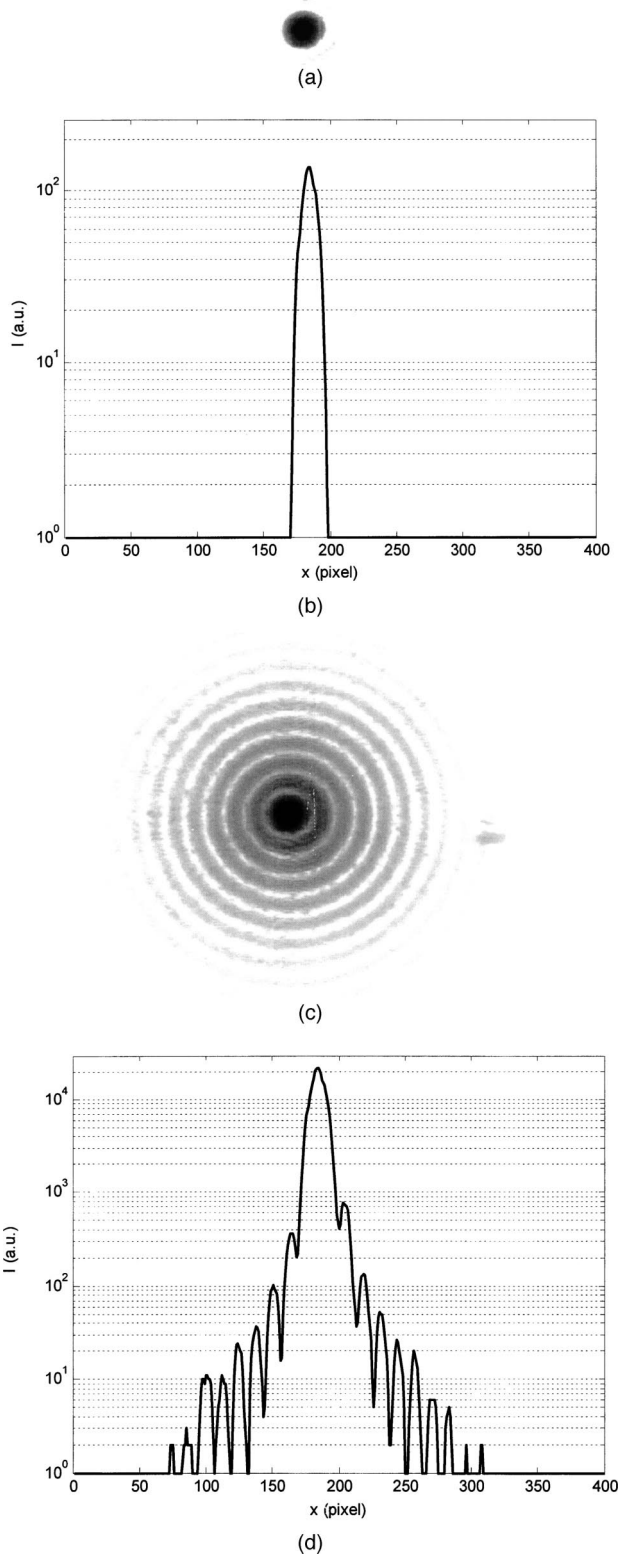


**Fig. 5** (a) Single digital image and (c) extended-irradiance-range image obtained for the diffraction pattern of a pinhole with a diameter of 200 $\mu$m. (b) and (d) show the corresponding profiles. All these images and curves are on a logarithmic scale.

We have also tried to eliminate the vertical structure before application of the extended-range technique. We generated a horizontal profile as the mean of the rows in the upper and lower regions of the image with the shortest

integration time, where the irradiance from the beam is negligible. Then, this horizontal profile was subtracted from all the rows of this image. After that, the extended range technique was applied once again. Figure 4 shows the principal widths obtained with the vertical smear removed as a function of the equivalent number of bits, $N_{eq}$. The dashed lines represent the asymptotic values obtained without removing the smear. It can be seen that the vertical width obtained with the second technique is slightly smaller (0.2%). Our interpretation of this result is that the extended-range technique greatly reduces the effect of the smear on the value of the vertical width, from 32% to 0.2%, but it cannot completely avoid this effect.

To show the performance of the method with a more structured image, we have measured the Fraunhofer diffraction pattern of a circular hole. Figure 5 shows the profile of the beam diffracted by a pinhole of 200-$\mu$m diameter back-illuminated by a stabilized HeNe laser. The CCD camera employed in this measurement was a progressive-scan black-and-white CCD camera, model JAI CV-M10, with a nominal dynamic range of 55 dB, equipped with electronic shutter with integration times $T_i = 1/50$, 1/125, 1/200, 1/500, 1/1000, 1/2000, 1/4000, and 1/10,000 s.

We observed the diffracted beam with a 50-mm objective focused to infinity; thus the digital images obtained correspond to the Fraunhofer diffraction pattern. Initially we set the integration time to 1/10,000 s, and we attenuated the laser beam with a rotating polarizer until the digital image observed presented no saturation. Figures 5(a) and 5(b) show the intensity distribution and its central horizontal profile, respectively, acquired for a single integration time of 1/10,000 s. The extended-range irradiance image and its profile are shown in Figs. 5(c) and 5(d). To get the image of Fig. 5(c), we used the full set of available integration times. Secondary diffraction maxima are visible up to order 9. As we know that the observed diffraction pattern must correspond to the Airy distribution, we can estimate the dynamic range for this irradiance image as 10,000:1, or 80 dB, much higher than the available dynamic range of the image acquisition system.

## 4 Conclusions

We have shown in this work that the application of the proposed extended-irradiance-range technique is a simple and cheap way to improve the accuracy of an off-the-shelf CCD-camera profiling system. There are two main reasons for this improvement. The first and more important one is that the increase of the dynamic range allows the acquisition of small irradiance values that would be lost if we acquired a single image. The second one is that for extended-irradiance-range images the background noise and the specific smear structures of each system lose importance compared to the irradiance distribution of the laser beam.

### *Acknowledgments*

This research was supported by the Comisión Interministerial de Ciencia y Tecnología under the projects DPI-2001/1369, DPI 2001/1238, and DPI2002-02104.

### *References*

1. C. B. Roundy, ''Electronic beam analysis of excimer lasers used for photorefractive keratotomy,'' *Proc. SPIE* **3405**(1–2), 673–685 (1998).
2. C. B. Roundy, ''Instrumentation for laser beam profile measurement,'' in *Laser Beam Characterization*, P. M. Mejías, H. Weber, R. Martinez-Herrero, and A. Gonzaléz-Ureña, Eds., pp. 215–226, SEDO, Madrid (1993).
3. B. C. Madden, ''Extended intensity range imaging,'' *Technical Report*, GRASP Lab., Univ. of Pennsylvania (1993).
4. P. E. Debevec and Jitendra Malik, ''Recovering high dynamic range radiance maps from photographs,'' in *SIGGRAPH 97 Conf. Proc.*, pp. 369–378 (1997).
5. M. A. Robertson, S. Borman, and R. L. Stevenson, ''Dynamic range improvement through multiple exposures,'' in *Proc. 6th Int. Conf. on Image Processing (ICIP'99)*, vol. 3, pp. 24–28 (1999).
6. G. C. Holst, *CCD Arrays, Cameras and Displays*, JCD Publishing and SPIE Optical Engineering Press (1996).
7. ''BeamStar user manual,'' *Technical Report*, Ophir Optronics Ltd. (2002).
8. International Organization for Standardization, ''Test methods for laser beam parameters,'' ISO/DIS 11146 (1999).
9. J. Alda, ''Laser and Gaussian beam propagation and transformation,'' in *Encyclopaedia of Optical Engineering*, R. B. Johnson and R. G. Driggers, Eds., Marcel Dekker, New York (2002).
10. J. Alda, J. Alonso, and E. Bernabeu, ''Characterization of aberrated laser beams,'' *J. Opt. Soc. Am.* **14**(10), 2737–2747 (1997).
11. J. Serna, ''Caracterización especial de haces luminosos bajo propagación a través de sistemas ópticos de primer order,'' PhD Thesis, Univ. Complutense de Madrid (1993).
12. A. Ghatak and K. Thygarajan, *Introduction to Fiber Optics*, Cambridge Univ. Press, New Delhi (1999).
13. J. Arines and J. Ares, ''Effective noise in thresholded intensity distribution: influence on centroid statistics,'' *Opt. Lett.* **26**(23), 1831–1833 (2001).
14. Wei Sun, Ghunqing Gao, and Guanghui Wei, ''Key factors in accurate beam characterization application,'' *Proc. SPIE* **4221**, 42–46 (2000).
15. Wei Sun, Ghunqing Gao, and Guanghui Wei, ''Processing application used in beam characterization,'' *Proc. SPIE* **4221**, 81–86 (2000).
16. C. B. Roundy, ''Techniques for accurately measuring laser beam width with commercial CCD cameras,'' in *Proc. 4th Int. Workshop on Laser Beam and Optical Characterization*, A. Giesen and M. Morin, Eds. (1997).

**R. González-Moreno** received his MSc degree in physics from the Universidad Complutense de Madrid, Spain, in 1999. Since October 1999 he has been a research fellow in the Departamento de Optica of the Universidad Complutense de Madrid. His research interests include image processing and metrology.

**J. A. Quiroga** received his MSc degree in 1989 and his PhD degree in physics in 1994, both from the Universidad Complutense de Madrid, Spain. He is now teaching in the Physics Faculty. His current principal areas of interest are digital image processing applied to the evaluation of fringe patterns and optical metrology.

**J. Alonso** received his MSc degree in 1988 and his PhD degree in physics in 1992 from the University Complutense of Madrid, Spain. He is now professor in the School of Optics of that university. His current principal areas of interest are ophthalmic optics and optical metrology.

**E. Bernabeu** received his MSc degree in 1966 and his PhD degree in 1969 in physics from the University of Zaragoza. He is now a professor in the Physics Faculty there. He has worked at l'Ecole Normale Superieure, at the Laboratoire de l'Horloge Atomique in Paris, at the International Center of Theoretical Physics of Trieste, and at the Universities of Zaragoza, Autonoma of Barcelona, and Complutense of Madrid. His previous research work was focused on quantum optics and molecular and atomic physics. Now his principal areas of interest are optoelectronics, optical sensors, fiber optical devices, and optical industrial inspection and metrology. He has written more than 200 papers and ten books about optical sensors, fiber optical devices, and optical-industrial inspection and metrology. He is member of OSA, and EPS.